applied optics

Dependence of spectral upwelling radiance distribution on optical properties and angular geometry in optically complex deep lakes

Yu Zhang,[1] Changping Huang,[2] Lifu Zhang,[2] Danling Tang,[1,*] and Qingxi Tong[2]

[1]Guangdong Remote Sensing Center for Marine Ecology and Environment (GDRS), Southern Marine Science and Engineering Guangdong Laboratory (Guangzhou), Guangzhou 511458, China
[2]Aerospace Information Research Institute, Chinese Academy of Sciences, Beijing 100094, China
*lingzistdl@126.com

Received 9 June 2026; revised 20 August 2026; accepted 23 August 2026; posted 24 August 2026; published 15 September 2026

The Q-factor is a key parameter characterizing the bidirectional structure of apparent optical properties, yet its variability in optically complex lakes has not been adequately characterized. This study quantitatively assesses and decouples the respective influences of inherent optical properties (IOPs) and angular parameters on the radiative regime, using data from 202 *in situ* stations with 208 $\tilde{b}_{bp}$ in Lake Taihu and over 30 million radiative transfer simulations. The results show that Q values range from 0.3 to 6.0 and Q-nadir (Q_n) exhibits spectral variations primarily driven by the particle backscattering ratio ($\tilde{b}_{bp}$), particularly in waters with an average number of collisions at 720 nm ($\bar{n}_{720}$) below 6.0 (Type 2 waters). In these waters, Q_n displays an inverted Gaussian pattern in the red spectral region (670–720 nm), likely associated with solar-induced chlorophyll fluorescence (SICF), and increases with $\tilde{b}_{bp}$, opposite to the trends observed at other wavelengths and in extremely turbid waters ($\bar{n}_{720} > 6.0$). Q increases with the solar zenith angle and decreases with increasing viewing zenith angle (θ_v). Coupled Q-factor models are proposed across the 400–750 nm spectral range at 5 nm intervals for optically deep lakes and yield R^2 values exceeding 0.85 and 0.71, with RMSE below 0.055 and 0.219 sr, respectively, when compared with Hydrolight simulated Q_n and Q-factor ($\theta_v \leq 60°$). Sensitivity analyses further reveal that wind speed and aerosol type have limited effects on Q_n, whereas isotropic SICF emissions in Type 2 waters suppress angular variability and induce a maximum relative difference of approximately 6.0% in Q_n at 680 nm. This study enhances the capability of multi-angle and hyperspectral remote sensing to model radiance distribution in optically complex deep lakes. © 2026 Optica Publishing Group. All rights, including for text and data mining (TDM), Artificial Intelligence (AI) training, and similar technologies, are reserved.

https://doi.org/10.1364/AO.608034

1. INTRODUCTION

Accurate characterization of radiance distribution, commonly described by the Q-factor, is essential for advancing multi-angle and hyperspectral remote sensing [1], particularly for understanding its anisotropic behavior in optically complex waters. It plays a critical role in accurate radiance retrieval, sensor calibration and validation, discrimination of optically complex waters, partitioning of water-leaving and atmospheric signals, and the integration of observations acquired under different viewing and illumination geometries [2–5]. Recent studies have shown that wavelength dependence has become a key factor limiting the accuracy of retrieval algorithms in inland waters [6], while traditional band-ratio approaches may not fully compensate for bidirectional effects. Moreover, the spectral range and angular coverage of existing Q-factor models remain insufficient to meet the demands of inland hyperspectral remote sensing. Therefore, a comprehensive understanding of the angular and spectral variability of the Q-factor is crucial for accurately deriving normalized water-leaving reflectance [2] and improving the retrieval of bio-optical parameters in optically complex aquatic environments.

Theoretical and experimental investigations of the Q-factor have mainly focused on oceanic and coastal waters. In Case 1 waters, molecular scattering is not negligible, and molecular backscattering may largely exceed particulate backscattering [7]. Q has been shown to vary strongly with chlorophyll concentration (Chl) as well as with solar and viewing geometry, leading to the development of precomputed lookup tables to quantify the variations of spectral radiances in waters with varying Chls ($\leq$10 mg/m^3) under different geometric conditions [8]. In sediment-dominated Case-2 waters, the contribution of molecular scattering becomes negligible, and radiance anisotropy

is mainly controlled by the particle phase function [2]. Previous studies further demonstrated that the upward radiance field remains anisotropic even in highly turbid waters and depends on solar geometry, water optical properties, and benthic conditions [3,9]. Although Zibordi and Berthon [1] measured nadir Q-factors (Q_n) at six spectral bands in the coastal waters of the North Adriatic Sea over solar zenith angles ranging from 20° to 80° and demonstrated that Q_n depends on the diffuse attenuation coefficient (K_d), solar zenith angle, and wavelength, their measurements were limited to nadir observations. Consequently, the angular distribution of the Q-factor beyond nadir still relies primarily on radiative transfer simulations. Moreover, most previous Q-factor studies were restricted to wavelengths below 670 nm and several discrete spectral bands. In contrast, inland lakes often retain relatively strong reflectance signals beyond 670 nm, which are critical for retrieving chlorophyll, suspended matter, and other water quality parameters [10,11]. Consequently, existing Q-factor models [1,8] remain insufficient for the demands of inland hyperspectral remote sensing and optically complex waters. Moreover, the distribution, spectral behavior, and potential applications of the Q-factor in optically complex inland lakes remain poorly understood.

Theoretically, as the average number of photon collisions before escaping from water ($\bar{n}$) increases and the single scattering albedo becomes sufficiently high, the upper layers of waters may approach a fully diffuse regime, with the upward radiance field becoming more isotropic [3]. In optically complex lakes, does the upward radiance field become less sensitive to the direction of incident light or viewing geometry, and how do the solar zenith angle and viewing angles influence its Q patterns under such conditions? The Q-factor is theoretically wavelength-dependent, yet its spectral variability remains relatively poorly understood in optically complex lakes. Finally, what parameters can best describe the relationship between the Q-factor and IOPs?

To investigate the upward radiance field distribution in optically complex lakes and address the questions above, we utilized extensive observational data from 202 *in situ* stations in Lake Taihu, 208 particle backscattering ratios ($\tilde{b}_{bp}$), and varying geometric configurations, along with over 30 million radiative transfer simulations. Based on these data and results, we developed semi-analytical models to establish quantitative frameworks describing the dependence of the Q-factor on geometry, wavelength, and IOPs, providing a robust foundation for characterizing radiance distributions and correcting bidirectional effects in optically complex lakes.

2. MATERIALS AND METHODS

A. Inland Waters IOPs and Radiative Transfer Simulations

Using Hydrolight 6.0 and *in situ* measurements from Lake Taihu as input, we generated a dataset of apparent optical properties (AOPs) representative of optically complex inland waters. The dataset includes measurements from Li *et al*. [12] in Meiliang Bay and from the National Earth System Science Data Center, National Science & Technology Infrastructure of China [13]. A four-component bio-optical model was used, comprising pure water, CDOM, non-algal particles (NAPs), and phytoplankton, denoted by the subscripts "w," "y," "NAP," and "ph," respectively. Detailed descriptions of the IOPs model and the radiative transfer framework for inland waters can be found by Zhang *et al*. [14] and are therefore not repeated here. In this study, phytoplankton and mineral particles were considered as independent scattering components. For phytoplankton particles, the particle backscattering ratio $\tilde{b}_{bp}^{c}$ at 555 nm was varied across 15 values (0.005–0.018 at 0.001 intervals, plus 0.0024) using Fournier–Forand (FF) phase function [15]. In addition, the Petzold [16] average volume scattering function (VSF) was included as a reference case, with a backscattering probability of 0.0183 at 555 nm. For mineral particles, the backscattering ratio $\tilde{b}_{bp}^{m}$ at 555 nm included 12 values (0.01–0.06 at 0.005 intervals and 0.013) using the FF phase function, together with the Petzold average VSF as an additional reference case. These ranges were chosen to adequately capture the variability in particle scattering properties in optically complex waters [17–19].

The radiative transfer equation (RTE) provides a rigorous framework to describe how the underwater radiative field is modified by and depends on the IOPs of the water [20]. It characterizes the variation of radiance magnitude and angular distribution with depth and can be accurately solved using Hydrolight 6.0 [21]. Due to the high concentration of suspended particulate matter (SPM), Lake Taihu exhibits an average Secchi depth of only 0.32 m. Therefore, only optically deep stations, where bottom influence is negligible, were used for radiative transfer simulations, assuming vertically uniform IOPs. To improve performance in optically complex waters, it is essential to expand the range of IOP variability considered in the radiative transfer simulations that form the basis of the BRDF lookup tables [2]. As shown in Table 1, the input inherent optical parameters used in this study for RTE simulations cover a wide range, with chlorophyll concentrations ranging from 1.79 to 98.43 mg/m^3 and TSM from 15.52 to 203.50 g/m^3. When combined with various backscattering ratios, these settings represent the majority of conditions found in optically complex waters. The rationale for this selection is to better understand and separately evaluate the influences of key parameters, such as the particle backscattering ratio and VSF, on the radiative regime by decoupling their variations. The VSF plays a key role in shaping radiance fields, as its angular distribution, particularly the backward scattering lobe, strongly influences the directionality of upwelling radiance and the resulting radiance anisotropy [22,23].

The simulations covered wavelengths from 400 to 800 nm under varying solar-viewing geometries (solar zenith angle,

Table 1. Summary of 202 Stations *In Situ* Data Collected from Lake Taihu

Parameters	Min	Max	Mean	Std
Water depth (m)	1.00	3.10	2.30	0.45
Temperature (°C)	3.4	31.0	17.8	8.7
Secchi depth (m)	0.10	0.65	0.30	0.10
TSM (g/m^3)	15.52	203.50	68.77	38.36
Chlorophyll-a (mg/m^3)	1.79	98.43	18.61	17.26
CDOM (440 nm, m^{-1})	0.41	0.55	0.48	0.044

viewing zenith angle, and relative azimuth angle) and particle backscattering conditions, without considering bottom effects. Other simulation settings, including wind speed and refractive index, followed those reported by Zhang *et al*. [14]. Surface roughness, sky radiance, atmospheric conditions, and inelastic scattering processes were included in the simulations.

B. Computation of Upwelling Radiance Distribution

The in-water radiance field in Lake Taihu was simulated using radiative transfer models with realistic IOPs and boundary conditions, where the upwelling flux at the surface constitutes a key component of the subsurface radiative field [24]. The upwelling radiance distribution function Q [25], defined as the ratio of the upwelling irradiance E_u to the upwelling radiance L_u in the zenith direction,

$$Q(\lambda, \theta_s, \theta', \varphi, \text{IOPs}) = E_u(0^-, \lambda, \theta_s)/L_u(0^-, \lambda, \theta_s, \theta', \varphi, \text{IOPs}) \quad [\text{sr}]. \tag{1}$$

The geometrical structure of the upwelling radiance field and its dependence on the illumination conditions above the surface, governed by the Sun's position, are both taken into account. In Eq. (1), θ' is the polar angle of the upwelling radiance direction and φ denotes the azimuth difference between the vertical plane containing the Sun and that containing the radiance L_u under consideration.

The spectral upward irradiance $E_u(0^-)$ just beneath the surface is defined as the integral of the upwelling radiance over upward directions, weighted by the cosine of the polar angle θ', with the azimuth angle ϕ varying from 0 to 2π [24]:

$$E_u(0^-) = \int_0^{2\pi} \mathrm{d}\phi \int_0^{\pi/2} L_u(0^-, \theta', \phi) \cos\theta' \sin\theta' \mathrm{d}\theta' \quad [\mathrm{W\,m^{-2}}]. \tag{2}$$

This study systematically quantifies the variations of the spectral Q-factor in inland waters by simulating various lake types with different IOPs under a range of geometric configurations, including the viewing zenith angle (θ_v), the solar zenith angle (θ_s), and the azimuth difference (φ) between the solar and viewing planes.

3. RESULTS

A. Analysis of Factors Influencing Q Patterns

The nadir-viewing Q-factor (Q_n), representing the Q-factor defined in Eq. (1) with $\theta' = 0$, was calculated through radiative transfer simulations in Lake Taihu and is shown in Fig. 1. All Q-factor values presented in this study are expressed in steradians (sr). Based on the average number of collisions at 720 nm ($\bar{n}_{720}$), the results are classified into Type 1 ($\bar{n}_{720} > 6.0$, representing extremely turbid waters) and Type 2 ($\bar{n}_{720} \leq 6.0$). Type 1 [Fig. 1(a)] waters show a Q_n maximum of 4.62 sr at 400 nm, a minimum of 3.93 sr at 722.5 nm, and an average of 4.29 sr, whereas Type 2 [Fig. 1(b)] waters exhibit a maximum of 4.62 sr at 400 nm, a minimum of 3.96 sr at 597.5 nm, and a mean of 4.28 sr. As shown in Figs. 1(a) and 1(b), Type 1 and Type 2 waters display distinct spectral features in the red region (670–720 nm), with Type 2 presenting a pronounced inverted Gaussian shape, partly associated with the contribution of chlorophyll fluorescence (see Section 4.C).

Q_n shows a slight decreasing trend with increasing $\bar{n}$ in Type 2 waters, whereas in Type 1 waters, Q_n slightly increases with $\bar{n}$ for $\bar{n}$ <5 and remains nearly unchanged when $\bar{n}$ exceeds 5. These different responses indicate that increasing photon collisions gradually alter the underwater radiance distribution, while Q_n becomes less sensitive to further increases in $\bar{n}$ in extremely turbid waters. This behavior is not only related to the average number of collisions but also closely linked to the VSF (Fig. 2), which is represented here by the particle backscattering ratio ($\tilde{b}_{bp}$), highlighting the strong dependence of the spectral upward radiance distribution on the inherent optical properties. As shown in Fig. 2, Q_n generally exhibited a decreasing trend with an increasing particle backscattering ratio across all wavelengths in most optically complex waters. However, Type 2 waters (represented by station S10) exhibited a distinct spectral response within the 660–700 nm range, where Q_n increased with increasing $\tilde{b}_{bp}$. This phenomenon is primarily related to the different photon interactions of chlorophyll and non-algal particles. The red region is particularly sensitive to phytoplankton absorption and chlorophyll fluorescence, with increasing chlorophyll concentration enhancing absorption and fluorescence while reducing the relative contribution of

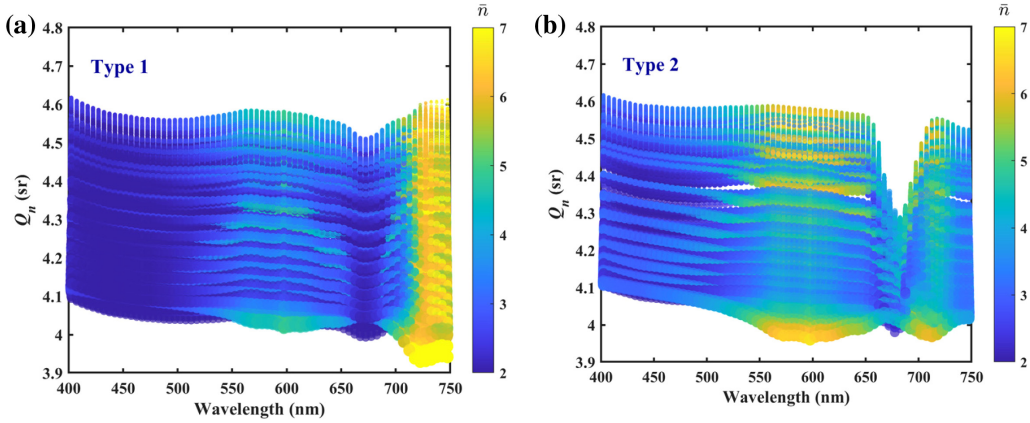


Fig. 1. Spectral variations of Q_n for (a) Type 1 and (b) Type 2 waters in Lake Taihu. Marker colors indicate $\bar{n}$, ranging from low values (blue) to high values (yellow), while marker sizes represent the relative contribution of $\tilde{b}_{bp}$.

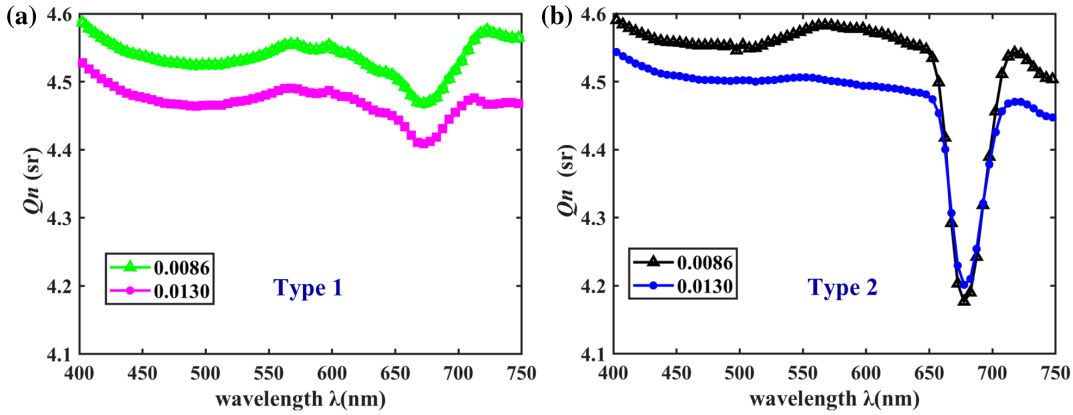


Fig. 2. Spectral variations of Q_n for (a) Type 1 and (b) Type 2 waters under different $\tilde{b}_{bp}$ conditions. Triangles indicate $\tilde{b}_{bp} = 0.086$, and circles indicate $\tilde{b}_{bp} = 0.013$.

backscattering [8]. Although enhanced absorption decreases the signal magnitude, the superimposed SICF signal becomes more influential for sensors with a larger full width at half-maximum of the relative spectral response function. This behavior reflects spatial differences in IOPs and the influence of the VSF and SICF on the inverted Gaussian amplitude. Accordingly, the spectral range for Type 2 was extended to 650–750 nm, within which Q_n consistently increased with increasing $\tilde{b}_{bp}$.

Q depends not only on inherent optical properties ($\bar{n}$ and $\tilde{b}_{bp}$) and wavelength but also on geometric configuration, including the solar zenith angle, viewing zenith angle, and relative azimuth angle. As shown in Figs. 3(a) and 3(b), Q_n values generally increase with the solar zenith angle for both Type 1 and Type 2 waters, particularly as the Sun approaches the horizon, consistent with previous theoretical and experimental studies [1,8,24,26]. These results confirm the positive correlation

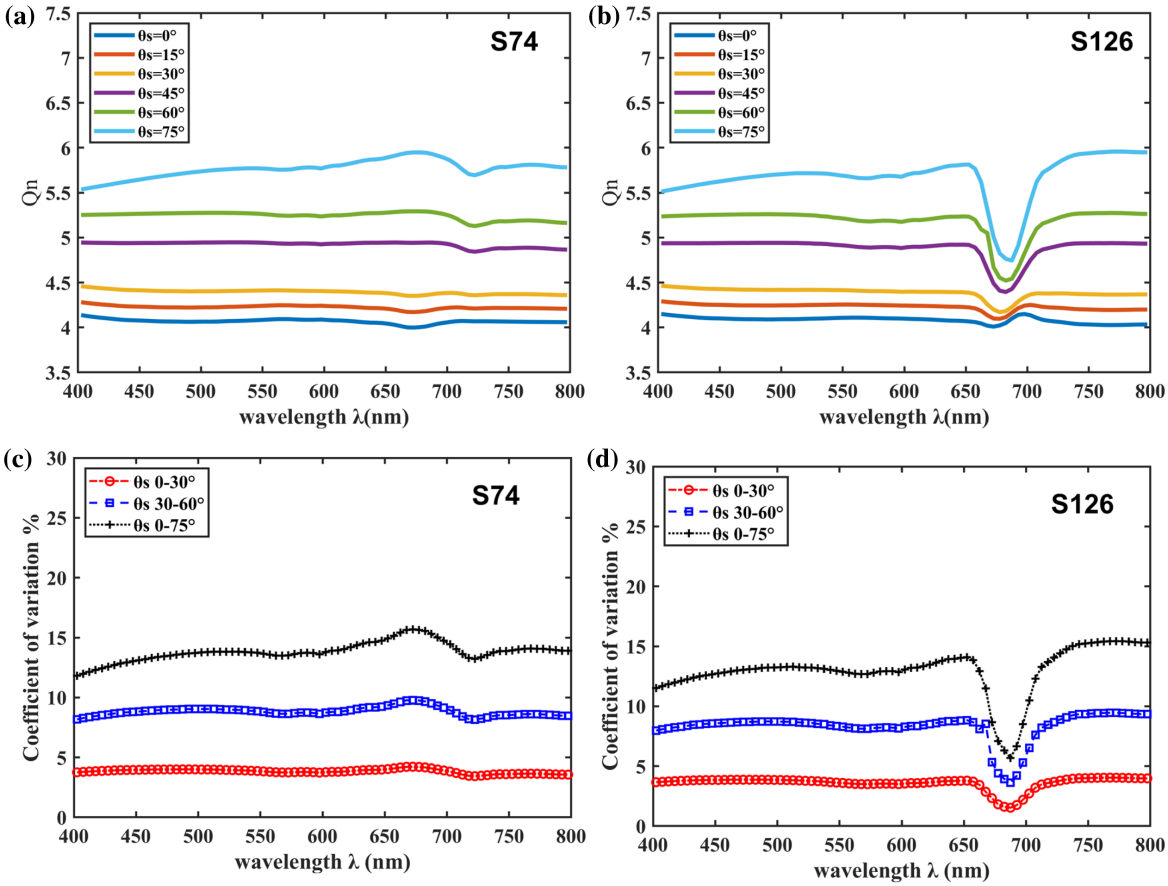


Fig. 3. Spectral variations of Q_n at different solar zenith angles for stations (a) S74 and (b) S126. Panels (c) and (d) show the corresponding coefficients of variation of Q_n across different solar zenith angle ranges at stations S74 and S126, respectively.

between Q_n and θ_s and extend the understanding of angular effects in optically complex deep lakes [Figs. 3(c) and 3(d)]. Specifically, when the solar zenith angle is below 30°, variations in Q_n are relatively minor, with coefficients of variation (CVs) less than 5%. Between 30° and 60°, the CV increases to around 8%, and across the full range from 0° to 75°, it reaches approximately 13%.

To analyze the variation of the Q-factor with viewing directions, Type 1 and Type 2 were selected, both characterized by a particle backscattering ratio of 0.0183 and a solar zenith angle of 30°. Polar plots of Q for these two cases are shown in Fig. 4 (Type 1) and Fig. 5 (Type 2) at eight wavelengths (412.5, 442.5, 487.5, 552.5, 662.5, 687.5, 717.5, and 757.5 nm). In optically inland waters, Q varies within the range of 0.1–6 sr.

The Q-factor consistently decreases with increasing viewing zenith angle, indicating a strong dependence on the viewing geometry. However, its variation with the relative azimuth angle is not strictly monotonic. A threshold behavior is observed at $\theta_v = 30°$: when $\theta_v \leq 30°$, Q increases with increasing φ, whereas when $\theta_v > 30°$, Q decreases as φ increases, under the solar zenith angle $\theta_s = 30°$. For Type 1 waters, the polar plots at the eight wavelengths exhibit consistent patterns, characterized by pronounced anisotropy in the angular distribution of Q. In contrast, Type 2 waters display a distinctive behavior

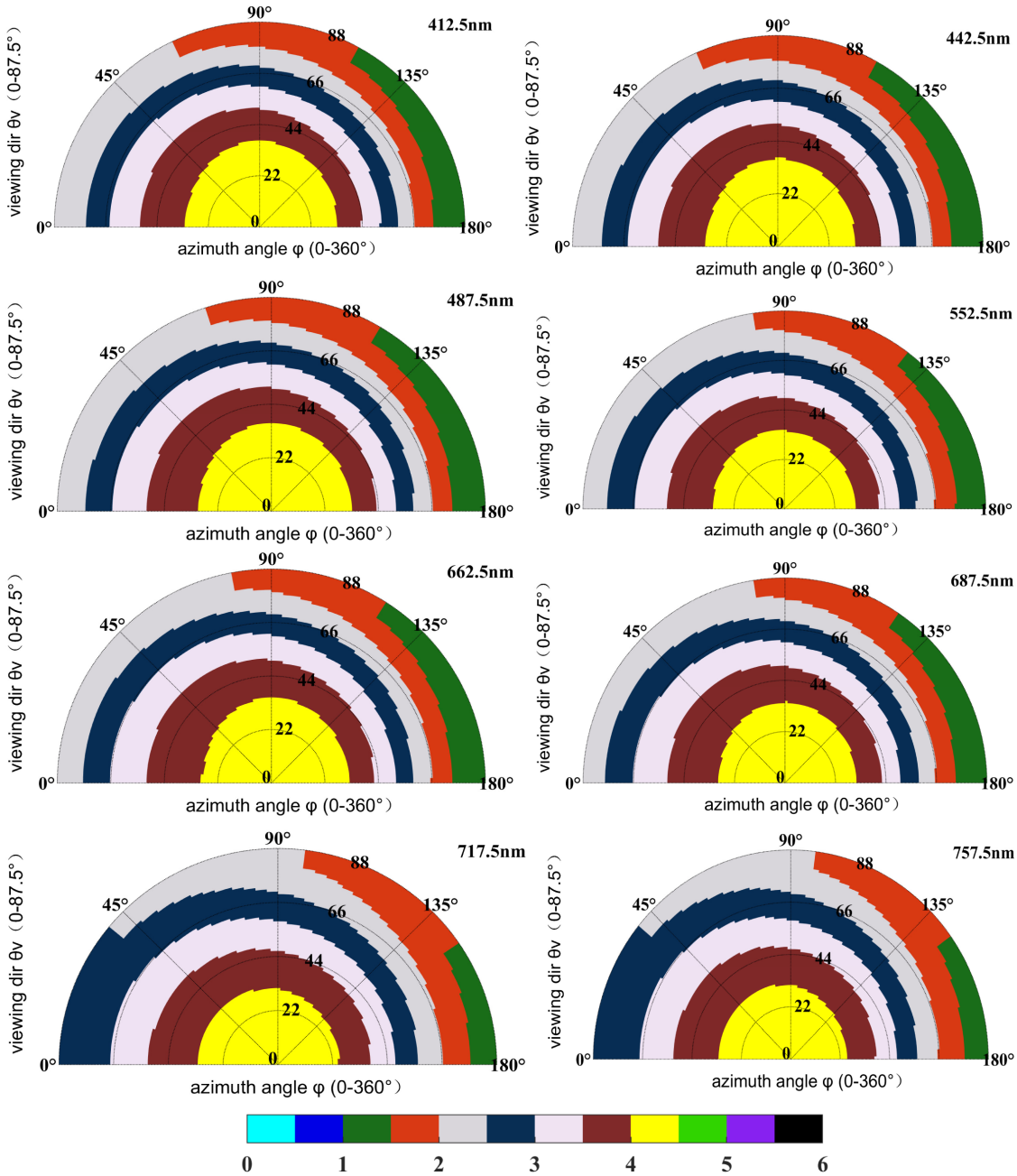


Fig. 4. Polar plots of Q as a function of viewing angles (0°−87.5°) and relative azimuth angles (0°−180°) at eight representative wavelengths (412.5, 442.5, 487.5, 552.5, 662.5, 687.5, 717.5, and 757.5 nm) for Type 1 waters (station S41, $\tilde{b}_{bp} = 0.0183$, $\theta_s = 30°$). The polar radius denotes the viewing angle, and the polar angle denotes the relative azimuth angle.

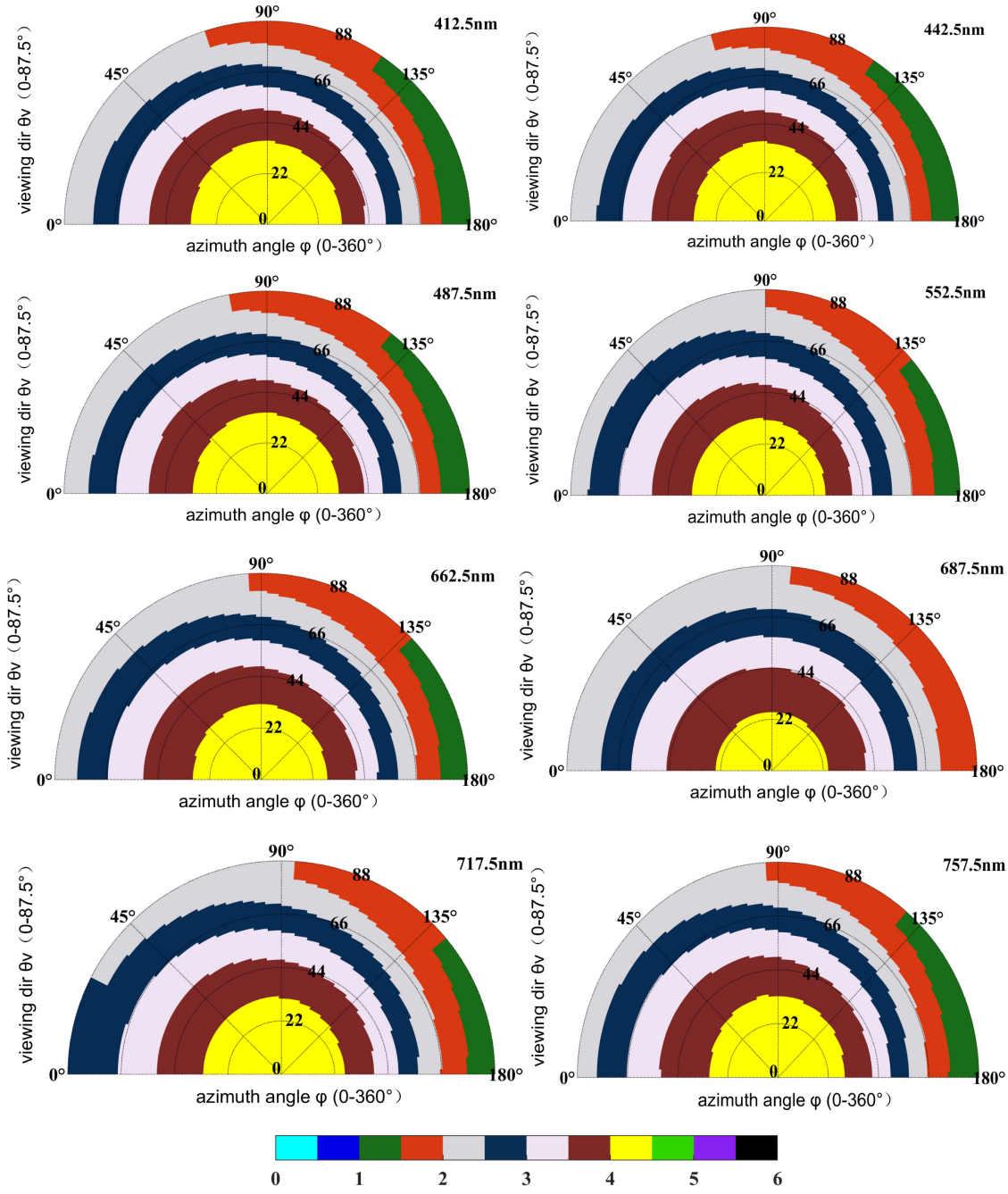


Fig. 5. Same as Fig. 4, but for Type 2 waters (station S10).

at 687.5 nm, where the sensitivity of Q to both the viewing zenith angle and the azimuth angle is reduced compared with other wavelengths, likely due to chlorophyll fluorescence, an inelastic and approximately isotropic emission that weakens angular variability. The similar angular patterns between Type 1 and Type 2 at other wavelengths are likely due to their strong particle backscattering. Although Type 2 (station S10) has a lower mineral concentration (30.56 g/m^3) than Type 1 (S41, 68.60 g/m^3), it remains a turbid case.

Notably, when θ_s is below 60°, Q tends to approach an isotropic distribution and be less sensitive to the illumination geometry. This characteristic is particularly relevant for applications relying on ratios of radiances at two wavelengths, which are generally far less affected by viewing geometry than individual radiances.

Overall, within this plane of symmetry, Q attains both its minimum and maximum values. The minimum ($Q_{\min}$) consistently appears in the horizontal direction, while the maximum ($Q_{\max}$) occurs in the vicinity of nadir, as previously reported by Morel and Gentili [4] and Morel *et al*. [27]. These results indicate that the viewing zenith angle generally dominates the variability of Q, while the influence of the azimuth angle

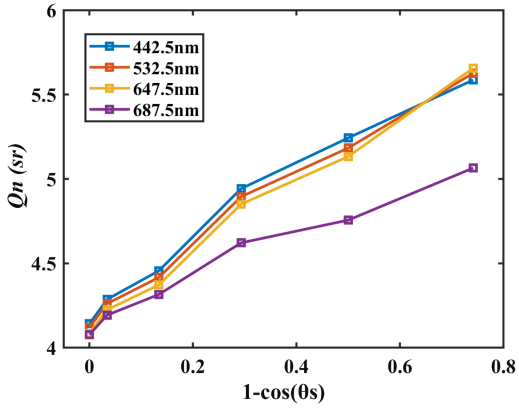


Fig. 6. Q_n as a function of $(1-\cos\theta_s)$ for four wavelengths (442.5, 532.5, 647.5, and 687.5).

becomes increasingly important at large viewing zenith angles ($>66°$).

B. Modeling the Upward Radiance Distribution

Considering the combined effects of the six variables (λ, θ_s, θ_v, φ, $\tilde{b}_{bp}$, and $\bar{n}$) in a single equation is not straightforward. Therefore, in this study, we first analyze Q_0, defined as the Q value under nadir illumination and nadir viewing conditions ($\theta_s=0°$, $\theta_v=0°$), followed by Q_n, and finally Q, using Q_n as the linking parameter. This sequential approach forms the foundation for modeling the upward radiance distribution. Figure 6 shows the relationship between Q_n and the solar zenith angle. At four representative wavelengths (442.5, 532.5, 647.5, and 687.5 nm), Q_n exhibited a strong linear correlation with $(1-\cos\theta_s)$. The slopes at 442.5, 532.5, and 647.5 nm were nearly identical, indicating similar sensitivity to changes in the solar zenith angle, whereas the slope at 687.5 nm was noticeably lower, suggesting that Q_n at this wavelength was less responsive to variations in θ_s. These findings further confirm the spectral dependence of Q [1].

Building on the observed relationship between Q_n and $(1-\cos\theta_s)$, a linear model describing Q_n as a function of the solar zenith angle was derived using the least-squares fitting method, as shown in Eq. (3):

$$Q_n(\theta_s,\lambda,\mathrm{IOPs}) = Q_0(0,\lambda,\mathrm{IOPs}) + S_{Qn}(\lambda,\mathrm{IOPs}) \times (1-\cos\theta_s), \tag{3}$$

where S_{Qn} represents the fitted slope describing the sensitivity of Q_n to changes in θ_s. The values of Q_0 and S_{Qn} are influenced by both wavelength and IOPs. Q_0 is systematically higher in inland waters, ranging from approximately 3.9 to 4.3 sr, compared to oceanic waters where it typically varies between 3.2 and 3.9 sr [24]. The values of S_{Qn} range from approximately 1.1 to 2.7, and Q_n values are generally smaller around 670–690 nm. This differs from the findings of Morel and Gentili [7,24], who reported the strongest variations in Q_n with the solar zenith angle at 670 nm, because in oceanic waters the single scattering albedo is low enough for single scattering to dominate the upward flux. In contrast, multiple scattering predominates in the Lake Taihu waters examined in this study.

After establishing the quantitative relationship between Q_n and the solar zenith angle, θ_s was fixed at 30°, and IOPs were varied. Through nonlinear least-squares fitting, quantitative expressions of Q_n as a function of $\tilde{b}_{bp}$ and $\bar{n}$ were derived for Type 1 waters, as shown in Eq. (4):

$$Qn(30,\lambda,\mathrm{IOPs}) = A1^{Q}\ln\tilde{b}_{bp} + B1^{Q}ln(\bar{n}(\lambda)) + C1^{Q} \quad \bar{n}_{720}>6.0, \tag{4}$$

where $A1^{Q}=-0.2773$, $B1^{Q}=0.0187$, and $C1^{Q}=3.2086$; λ ranges from 400 to 750 nm. This expression indicates that, in highly turbid waters, Q_n decreases with increasing $\tilde{b}_{bp}$ due to enhanced multiple scattering, while it slightly increases with higher $\bar{n}$, reflecting the influence of the photon path length on the angular distribution of upward radiance.

For Type 2 waters, the relationship within the 400–650 nm range follows the same functional form as that in Eq. (4), whereas in the 650–750 nm range, Q_n exhibits an inverted Gaussian-like dependence. The model for Type 2 waters is presented in Eq. (5):

$$Qn(30,\lambda,\mathrm{IOPs}) = A2^{Q}\ln\tilde{b}_{bp} + B2^{Q}ln(\bar{n}(\lambda)) + C2^{Q} \quad 400-650\ \mathrm{nm}\quad \bar{n}_{720}\le 6.0, \tag{5a}$$

$$Qn(30,\lambda,\mathrm{IOPs}) = a^{Q}e^{-\left(\frac{\lambda-\lambda_0}{b^{Q}}\right)^2} + c^{Q} \quad 650-750\ \mathrm{nm}, \tag{5b}$$

where $A2^{Q}=-0.3042$, $B2^{Q}=-0.0415$, and $C2^{Q}=3.2206$ for the 400–650 nm range; and $\lambda_0=679.5\pm6.0$, $a^{Q}=0.1419\pm0.1436$, $b^{Q}=15.2905\pm23.3447$, and $c^{Q}=4.2701\pm0.1686$ for the 650–750 nm range. Equation (5) indicates that in waters characterized by moderate to low turbidity, which account for the majority of the investigated cases, both $\tilde{b}_{bp}$ and $\bar{n}$ have negative effects on Q_n. Eq. (5) indicates that where Q_n slightly increases with $\bar{n}$, indicates that Q_n decreases marginally with increasing photon collisions, reflecting a radiance field still dominated by limited multiple scattering. Overall, regardless of whether the water is Type 1 or Type 2, $\tilde{b}_{bp}$ is the dominant factor controlling the distribution of upward radiance.

The variations of Q with θ_v and φ were described in Section 3.A: Q decreases with increasing θ_v; when θ_v is between 0° and 30°, Q increases with increasing φ; and when θ_v is between 30° and 90°, Q decreases as φ increases. Based on these established trends, and noting that anisotropy becomes more pronounced at $\theta_v>60°$, nonlinear least-squares fitting was applied to Eq. (6) for different θ_v ranges to determine the coefficients K^{Q}, T^{Q}, and P^{Q}, with the resulting values shown in Table 2:

$$Q(30,\theta_v,\varphi) = K^{Q}Q_n + T^{Q}\sin\theta_v + P^{Q}\cos\varphi. \tag{6}$$

The coefficients T^{Q} and P^{Q} in Table 2 further show the dependence of Q on θ_v and φ. When $\theta_v<30°$, the effect of φ on Q patterns is relatively small, whereas for $\theta_v>60°$, the influence of φ becomes more pronounced. Overall, the impact of the viewing zenith angle is substantially greater than that of

Table 2. K^Q, T^Q, and P^Q Values of Q-Factor Look-Up Table

θ_v	Values		
	K^Q	T^Q	P^Q
0°−30°	1.0293	−0.8463	−0.0428
30°−60°	1.3364	−3.2308	0.2338
60°−87.5°	0.7532	−1.3072	0.5246

the relative azimuth angle. These conclusions, derived from the three fitted parameters, are fully consistent with the patterns shown in Figs. 4 and 5. This piecewise fitting approach allows reasonably accurate representation of the Q-factor across all viewing geometries, capturing the enhanced anisotropy at high zenith angles.

Finally, the upward radiance distribution in optically complex deep lakes was expressed as a function of six variables (λ, θ_s, θ_v, φ, $\tilde{b}_{bp}$, and $\bar{n}$) and quantitative expressions were derived [Eqs. (3)–(6)]. These formulations allow for a reasonably accurate representation of the Q-factor, providing a robust foundation for the observation and understanding of upward radiance fields in inland waters, as well as establishing a theoretical basis for quantitative retrievals.

C. Assessments with Hydrolight Data

The model results were compared with Hydrolight simulations, and the evaluation of Q_n with respect to the solar zenith angle and IOPs is shown in Figs. 7 and 8. Model performance was evaluated using the coefficient of determination (R^2) and the root mean square error (RMSE). As shown in Fig. 7, our model describing the relationship between the solar zenith angle and Q_n shows high accuracy, with an R^2 of 0.99 and a low RMSE of 0.0660 sr compared with Hydrolight simulations. This result indicates that the influence of the solar zenith angle on the upward radiance distribution function can be accurately characterized and effectively corrected at the nadir viewing direction.

For extremely turbid waters [Fig. 8(a)], the modeled and Hydrolight derived Q_n values ranged from 4.0 to 4.8. A total of 160,160 samples were used for comparison, yielding

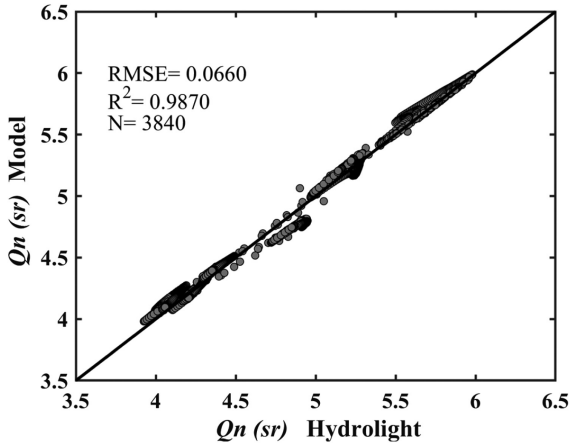


Fig. 7. Comparison of Q_n values derived from Eq. (3) with Hydrolight simulations as a function of the solar zenith angle across the 400–800 nm spectral range at representative stations.

$R^2 = 0.8506$ and RMSE = 0.0545 sr. The residual histogram is shown in Fig. 8(b), with resnorm representing the residual sum of squares. Differences between the modeled and simulated Q_n values were mostly within −0.1 to 0.1, with a slight overestimation around at 4.1 sr and slight underestimation at higher values. Overall, these results demonstrate that the proposed model performs well in highly scattering environments, effectively capturing the distribution of upward radiance. In Type 2 waters, comparisons with 131,000 Hydrolight simulated samples yielded R^2 values exceeding 0.95 and an RMSE below 0.034 sr. The residuals were tightly clustered between −0.05 and 0.05 sr, and the residual histograms approximate a normal distribution, indicating excellent agreement between the modeled and simulated values. These results demonstrated that the proposed formulations [Eqs. (5a) and (5b)] robustly capture the angular variability of Q_n across both the 400–650 nm and 650–750 nm spectral ranges. Unlike extremely turbid waters (Type 1), Type 2 waters show higher sensitivity to IOPs, yet the model effectively reproduces the upward radiance distribution across the entire spectrum.

Figure 9 compares the Q-factor values derived from the proposed model [Eq. (6)] with those simulated by Hydrolight, along with the corresponding residual distributions. Based on more than 10 million data, the model achieved high accuracy at viewing zenith angles below 30° [Figs. 9(a) and 9(b)], yielding an R^2 of 0.8943 and an RMSE of 0.0609 sr. The residual histogram followed an approximately normal distribution, confirming the model's reliability in this angular range. For viewing zenith angles between 30° and 60° [Figs. 9(c) and 9(d)], the model performance remained acceptable, with $R^2 = 0.7158$ and RMSE = 0.2183 sr. However, when the viewing zenith angle exceeded 60° [Figs. 9(e) and 9(f)], model accuracy decreased noticeably, with R^2 dropping to 0.5076 and RMSE increasing to 0.3612 sr. This decrease in model accuracy under large viewing zenith angles is attributed to the enhanced anisotropy of the radiance field, which becomes more pronounced under oblique observation conditions. Overall, the coupled Q-factor model provides a reasonably accurate representation of the upward radiance distribution for $\theta_v \leq 60°$, while further optimization is required to better account for the complex anisotropy effects at larger viewing angles.

4. DISCUSSION

A. Impact of Bottom Reflectance

Although benthic substrate effects are not considered in this study due to the assumption of optically deep waters, they may introduce additional uncertainty when extending the proposed parameterization to optically shallow environments. To evaluate bottom effects and model applicability in optically shallow waters, we analyzed the Q_n spectra for five representative bottom types (clean seagrass, macrophyte, seagrass, hardpan, and ooid sand) at station N25 in Nansi Lake [14], using $\tilde{b}_{bp} = 0.014$ as an example [Fig. 10(a)]. The bottom reflectance data were obtained from field measurements of coastal seabed optical properties near Lee Stocking Island, Bahamas [21]. The results showed that Q_n was negligibly affected by the bottom type at wavelengths below 525 nm, since light in the 400–525 nm

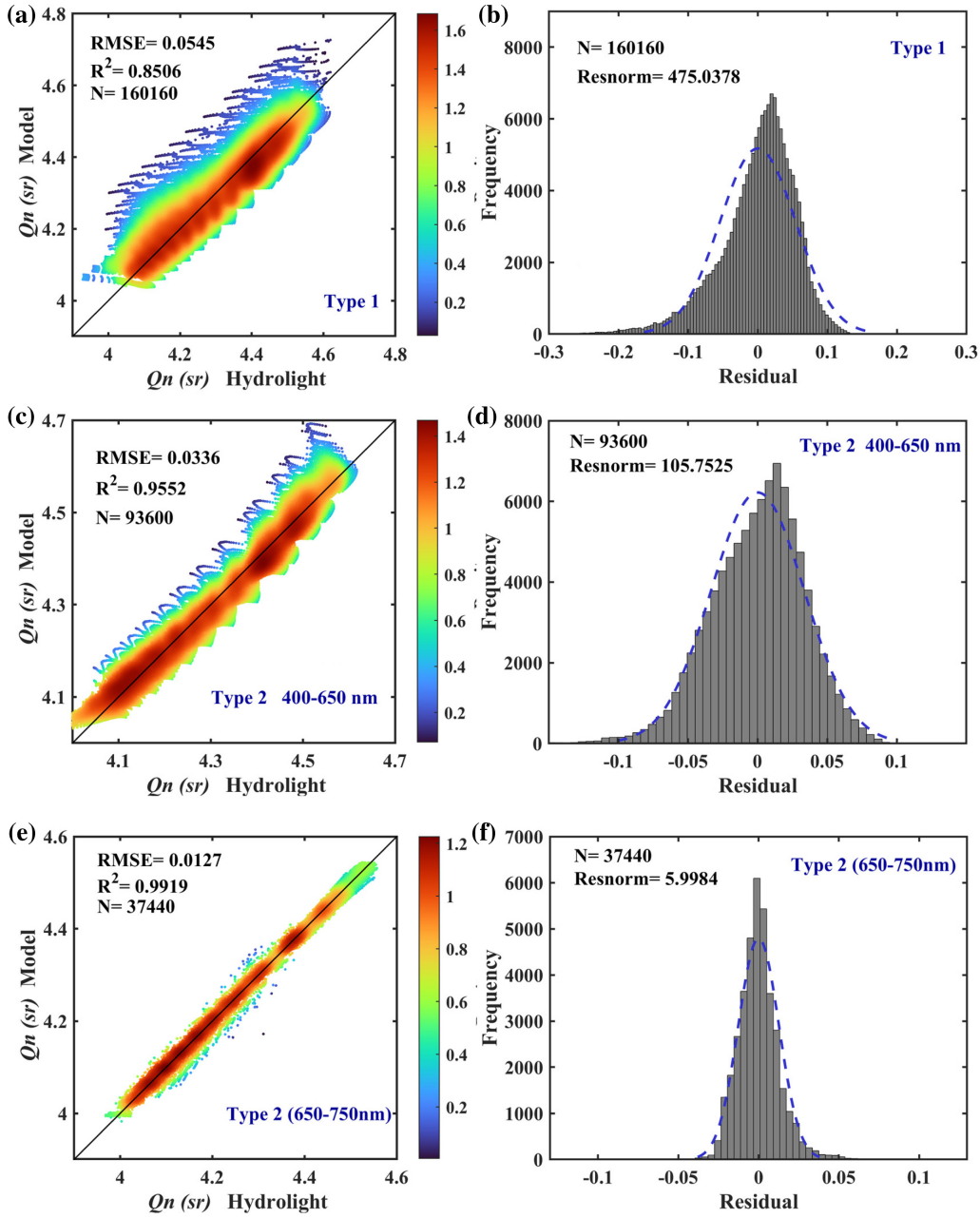


Fig. 8. Comparison of Q_n values derived from Eqs. (4) and (5) with Hydrolight simulation results (a), (c), and (e), and the corresponding residual histograms (b), (d), and (f) for Type 1 and Type 2 waters, where the x axis represents the residuals and the y axis represents the number of samples: (a) and (b) Type 1 waters (400–750 nm); (c) and (d) Type 2 waters (400–650 nm); and (e) and (f) Type 2 waters (650–750 nm).

range is strongly attenuated within the water column due to absorption by CDOM and phytoplankton pigments, and thus contributes little to bottom-reflected radiance. In contrast, the influence of the bottom type became evident in the spectral ranges of 550–650 nm and 690–750 nm, where the coefficients of variation exceeded 5% and 10% [Fig. 10(b)], respectively, with two distinct peaks near 600 and 720 nm. This is attributed to the stronger penetration of green light and the higher bottom reflectance in these spectral regions.

In these spectral regions, bottom effects on radiance distribution were particularly pronounced and could introduce uncertainties in the retrieval of water quality parameters such as chlorophyll and SPM. Therefore, bottom contributions should be accounted for or corrected when applying optical models in optically shallow waters. Conversely, the coefficients of variation within 400–550 nm and 650–680 nm remained below 2%, confirming that bottom influence in these wavelength ranges is minimal. However, it should be noted that this conclusion is derived from radiative transfer simulations and has not yet been validated by *in situ* measurements. Furthermore, variations in water type and the VSF may affect this conclusion, and thus further investigation is required.

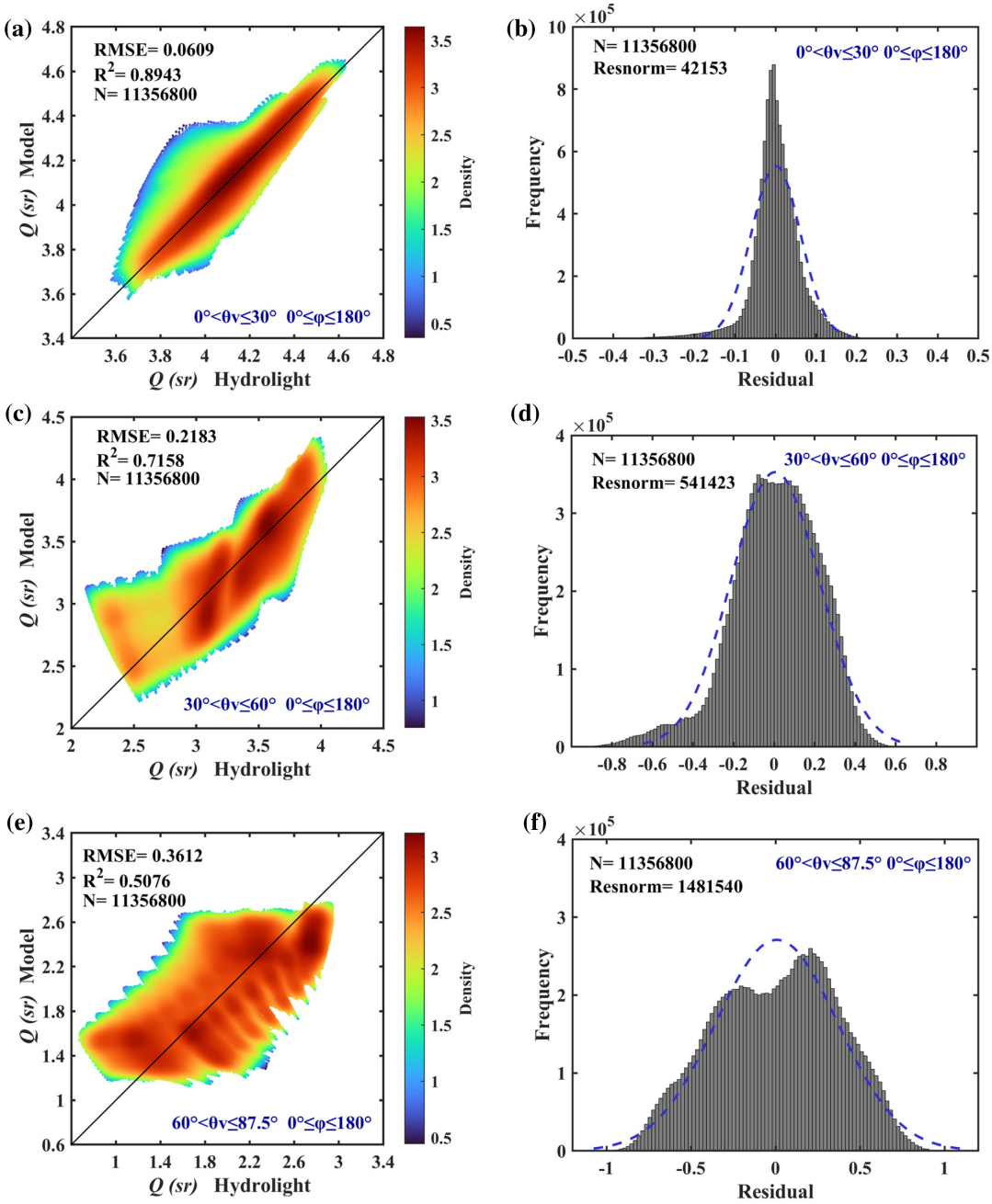


Fig. 9. Comparison of the Q-factor at different viewing angles between Eq. (6) and the Hydrolight simulations (a), (c), and (e), and the corresponding residual histograms (b), (d), and (f): (a) and (b) $0 \le \theta_v \le 30°$, (c) and (d) $30 < \theta_v \le 60°$, and (e) and (f) $60 < \theta_v \le 87.5$.

B. Anisotropy of Upward Radiance at High Solar Zenith Angle

To further investigate the behavior of the Q-factor under extreme angular conditions, station S6 in Lake Taihu was analyzed with a solar zenith angle of 68° and of $\tilde{b}_{bp}$ 0.013. The remaining IOPs were set according to Li *et al*. [12]. Radiative transfer simulations under these conditions produced the polar Q distribution shown in Fig. 11, with values ranging from 0.5 to 6.0 sr, reflecting enhanced anisotropy relative to simulations at a 30° solar zenith angle. As shown in Fig. 11, at large solar zenith angles, Q decreases with increasing viewing zenith and relative azimuth angles. Notably, the threshold previously observed at a θ_v of 30°, which separated different behaviors of relative azimuth angle influence, no longer applies. This shift is primarily due to the elevated Q-factor values associated with higher solar zenith angles, which amplify angular anisotropy. Moreover, Q values are systematically higher at relative azimuth angles between 0°–90° than at 90°–180°, causing a leftward shift of the polar symmetry center. This pattern reflects enhanced forward scattering under these conditions, because particulate scattering in aquatic media is inherently highly forward-peaked. At large solar zenith angles, the increased optical path length rapidly attenuates the direct solar beam, making

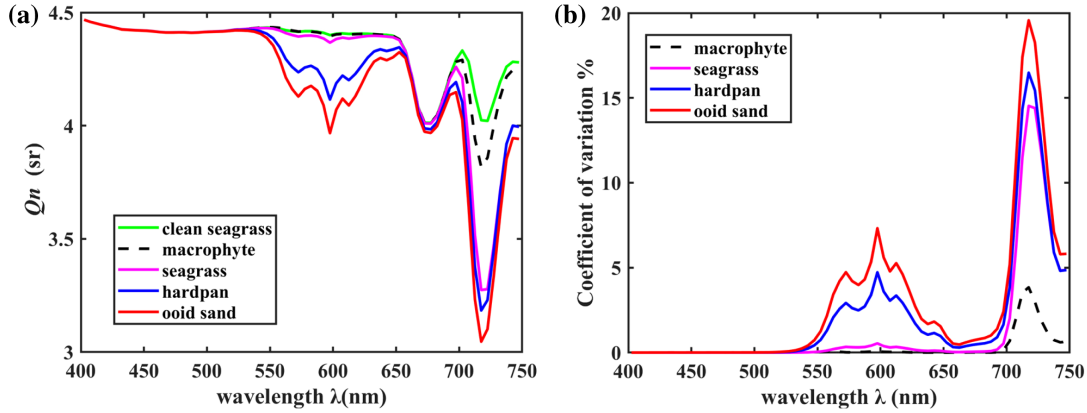


Fig. 10. (a) Q_n spectra for five bottom types—clean seagrass, macrophyte, seagrass, hardpan, and ooid sand ($\tilde{b}_{bp} = 0.014$) at station N25 in Nansihu Lake; (b) coefficients of variation of Q_n for four bottom types relative to clean seagrass at the same station.

this forward-scattered diffuse light the dominant component of the downwelling light field.

The bidirectional structure of AOPs becomes increasingly pronounced at high solar zenith angles, even for small viewing zenith angles. This highlights the critical importance of accurate BRDF correction in optically complex waters under extreme solar illumination. Reliable characterization of normalized water-leaving radiance under these conditions is essential for precise retrieval of water quality parameters and for advancing the understanding of optical properties, biogeochemical processes, and the development of robust remote sensing algorithms in inland and coastal waters.

C. Accounting for Other Variables

The geometric structure of the downward irradiance field and the resulting upward radiance distribution can be influenced by surface wave slopes, which are related to wind speed (W). In principle, this suggests that Q could be sensitive to variations in W. As shown in Fig. 12(a), Hydrolight simulations incorporating the Cox–Munk model [28] under different wind speeds (5–15 m/s) show that Q_n increases slightly with wind speed, with relative differences of 1.0%–1.6% (slightly larger in the blue region at ~1.5%). In addition, the Q-factor is theoretically influenced by aerosol optical depth (AOD) as atmospheric turbidity alters the balance between direct and diffuse irradiance reaching the water surface [2,24]. Figure 12(b) shows the effect of three aerosol types on Q_n; the mean absolute relative difference between marine and continental aerosols is less than 1% across the entire spectrum. This result is consistent with Morel and Gentili [24], indicating that the effect of AOD on Q is secondary compared with the dominant influence of in-water absorption and scattering processes. Interestingly, around 510 nm, the relative influence of aerosol types changes, with marine aerosols producing lower Q_n values in the blue region but slightly higher values in the green-to-NIR region. This spectral behavior may result from the combined effects of aerosol scattering properties, spectral irradiance redistribution, and wavelength-dependent water absorption. Compared with continental fine-mode aerosols, marine aerosols containing larger sea-salt particles generally exhibit stronger forward scattering and weaker spectral variability, which may contribute to the observed crossover behavior near 510 nm. This analysis focuses on the underwater Q-factor under optically deep conditions; surface roughness and diffuse skylight effects should be considered when extending the model to above-water and coastal applications [29].

As shown in Fig. 12(c), the fluorescence effect on Q_n is water-type dependent. In extremely turbid waters (Type 1), multiple scattering by high particle concentrations suppresses the fluorescence signal, making its contribution negligible. In Type 2 waters, however, the fluorescence signal is more detectable and exerts a discernible influence on Q_n, with a maximum relative difference of approximately 6.0% at 680 nm. This suggests that in eutrophic or high-fluorescence waters, fluorescence effects on Q_n in the red band should be considered in BRDF correction schemes, as accounting for chlorophyll fluorescence can improve radiometric closure in these spectral regions [30]. Therefore, fluorescence effects were explicitly retained in our radiative transfer simulations and accounted for in the inverted Gaussian Q-factor model developed for Type 2 waters in the 650–750 nm region.

D. Q_n Validation Using Field Data

Figure 13 shows the Q_n data collected by Zibordi and Berthon [31] in optically complex waters (Baltic Sea and North Sea) on clear-sky days. Across the six stations, chlorophyll-a ranged from 1.002 to 5.862 μg/L and SPM from 0.95 to 2.05 g/m^3. While the SPM concentrations are substantially lower than those in the optically deep lakes investigated here, the dataset nevertheless serves as a valuable independent test for examining Q_n behavior and corroborating the model predictions. A clear dependence on the solar zenith angle is observed: stations with larger zenith angles (N010501, N010701, and B011501) show Q_n values of about 5.5 sr, significantly higher than ~4.5 sr found at stations with smaller zenith angles (N010201, N010301, and N010401). Furthermore, at N010201 and N010301, where solar zenith angles are nearly identical, Q_n decreases with increasing $\tilde{b}_{bp}$ and $\bar{n}$, which is generally consistent with the findings of this study.

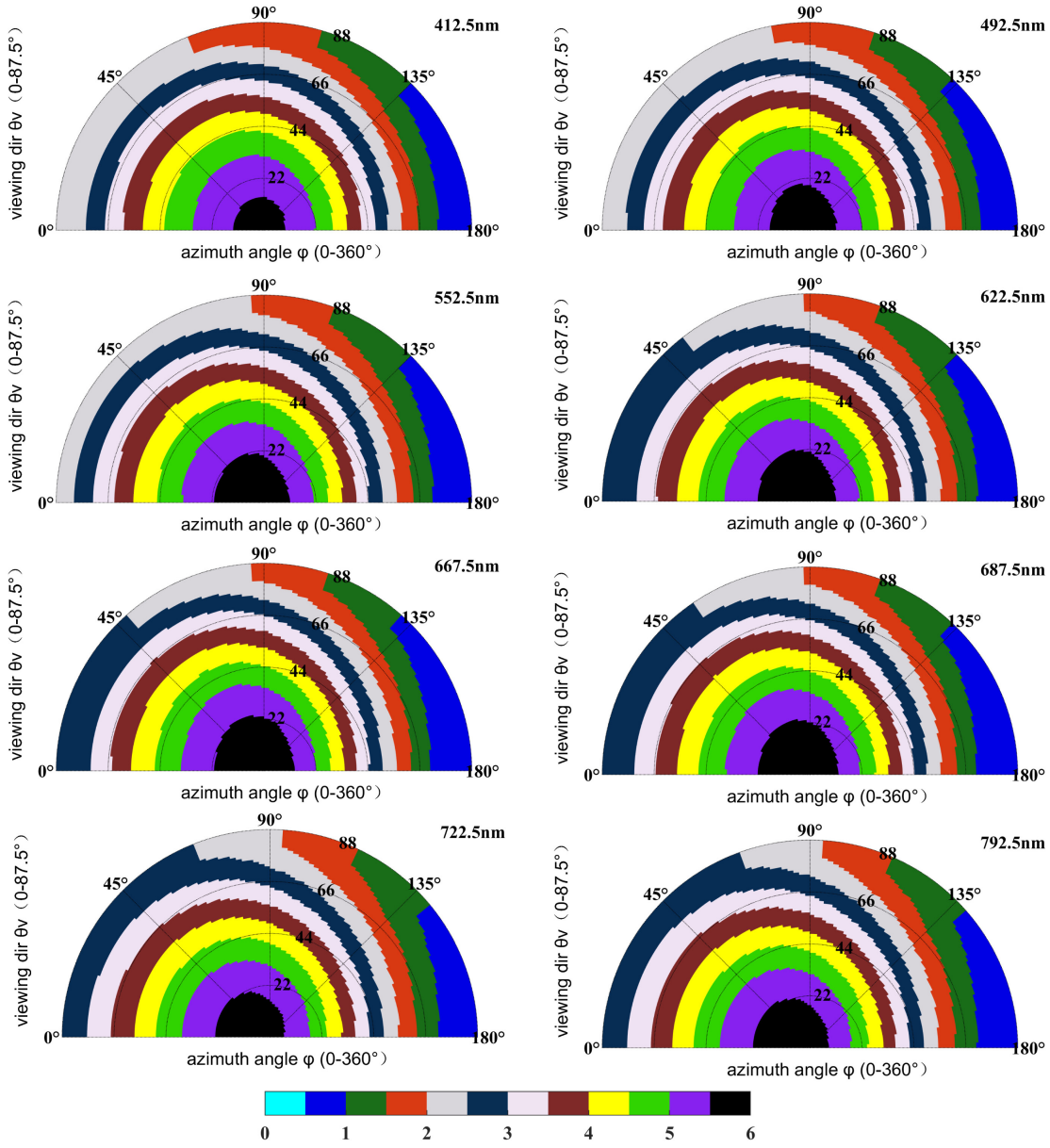


Fig. 11. Q-factor distribution as a function of viewing geometry at a large solar zenith angle (S6 station, $\theta_s = 68°$, $\tilde{b}_{bp} = 0.013$) across eight wavelengths: 412.5, 492.5, 552.5, 622.5, 667.5, 687.5, 722.5, and 792.5 nm.

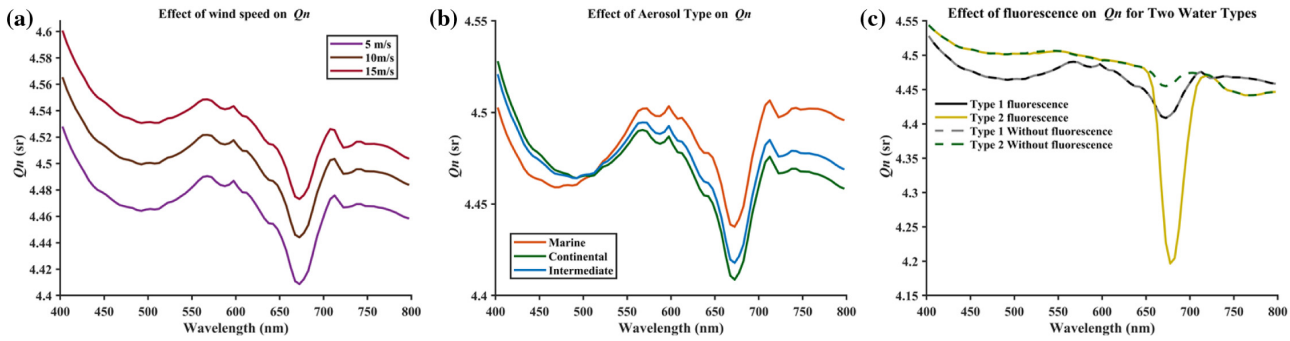


Fig. 12. Simulated Q_n spectra illustrating the effects of (a) wind speed, (b) aerosol type, and (c) fluorescence.

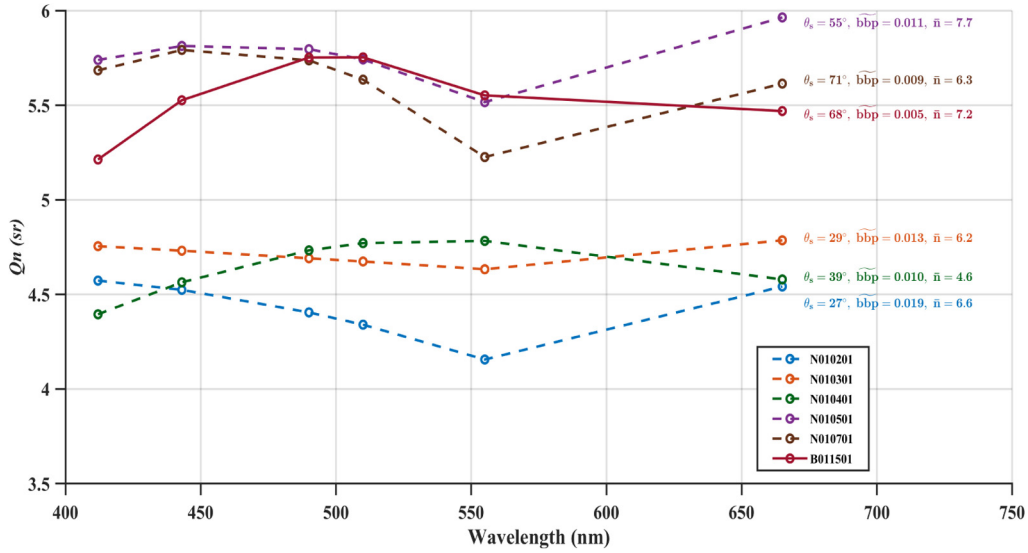


Fig. 13. *In situ* Q_n spectra measured at N01 (North Sea, dashed) and B01 (Baltic Sea, solid) stations.

Using N010301 in Eq. (5a), the modeled Q_n values are 4.48 and 4.51 sr at 510 and 555 nm, leading to differences of 4.07% and 2.59% against *in situ* values of 4.67 and 4.63 sr, demonstrating that the model provides reasonably accurate estimates despite a slight systematic underestimation.

Previous studies have relied on radiative transfer simulations and a single or simplified backscattering probability assumption, while field measurements have largely been limited to indirect estimates of Q-nadir. As a result, the angular distribution and variability of the Q-factor remain insufficiently understood, particularly in optically complex inland waters. This study provides important insight into the variability of Q and its controlling factors through extensive radiative transfer simulations constrained by *in situ* measurements.

5. CONCLUSION

This study investigated the upwelling radiance distribution in optically complex inland waters and demonstrated that geometry (solar zenith angle and viewing angles), wavelength, and IOPs remain key factors shaping Q patterns. Using *in situ* optical measurements and over 30 million radiative transfer simulations, a semi-analytical Q-factor model was developed with Q_n as a linking parameter and incorporating six variables ($\lambda, \theta_s, \theta_v, \varphi, \tilde{b}_{bp}$, and $\bar{n}$). Validation against Hydrolight simulations showed strong consistency ($R^2 > 0.89$, RMSE < 0.06 sr for $\theta_v \leq 30°$; $R^2 > 0.72$, RMSE < 0.22 sr for $30°-60°$). In addition, by fully accounting for variations in backscattering probability and addressing the spectral dependence and anisotropy of Q within the 670–750 nm range, the model effectively characterizes the role of VSF and spectral behavior in optically complex inland waters, which are often negligible in oceanic and coastal environments where upwelling radiance beyond 670 nm is weak. This study presents the first quantitative characterization of the combined effects of viewing geometry and IOPs on Q in inland waters, providing a foundation for future hyperspectral and multi-angle remote sensing to improve retrievals of biogeochemical components and account for bidirectional effects. Future work should focus on collecting field measurements of E_u, L_u, and VSF to validate the Q-nadir model.

Funding. National Key Research and Development Program of China (2024YFE0114300); Guangdong Special Key Talents Team Program (2019BT02H594); PI Project of Southern Marine Science and Engineering Guangdong Laboratory (Guangzhou) (GML2021GD0810).

Acknowledgment. Thanks for the data support from "Lake-Watershed Science Data Center, National Earth System Science Data Center, National Science & Technology Infrastructure of China [13]".

Disclosures. The authors declare no conflicts of interest.

Data availability. Data underlying the results presented in this paper are available in Ref. [13].

REFERENCES

1. G. Zibordi and J.-F. Berthon, "Relationships between Q-factor and seawater optical properties in a coastal region," Limnol. Oceanogr. **46**, 1130–1140 (2001).
2. D. DAlimonte, T. Kajiyama, J. Pitarch, *et al.*, "Comparison of correction methods for bidirectional effects in ocean colour remote sensing," Remote Sens. Environ. **321**, 114606 (2025).
3. H. Loisel and A. Morel, "Non-isotropy of the upward radiance field in typical coastal (Case 2) waters," Int. J. Remote Sens. **22**, 275–295 (2001).
4. A. Morel and B. Gentili, "Diffuse reflectance of oceanic waters. II. Bidirectional aspects," Appl. Opt. **32**, 6864–6879 (1993).
5. K. J. Voss, "Use of the radiance distribution to measure the optical absorption coefficient in the ocean," Limnol. Oceanogr. **34**, 1614–1622 (1989).
6. Y. Zhang, L. Zhang, Y. Cen, *et al.*, "The f'/Q factor in the relationship between inherent and apparent optical properties in a Typical inland Water (Lake Taihu, China)," IEEE J. Sel. Top. Appl. Earth Obs. Remote Sens. **17**, 1565–1574 (2024).
7. A. Morel and B. Gentili, "Diffuse reflectance of oceanic waters: its dependence on Sun angle as influenced by the molecular scattering contribution," Appl. Opt. **30**, 4427–4438 (1991).

8. A. Morel, D. Antoine, and B. Gentili, "Bidirectional reflectance of oceanic waters: accounting for Raman emission and varying particle scattering phase function," Appl. Opt. **41**, 6289–6306 (2002).
9. K. J. Voss, C. D. Mobley, L. K. Sundman, *et al.*, "The spectral upwelling radiance distribution in optically shallow waters," Limnol. Oceanogr. **48**, 364–373 (2003).
10. R. S. Gupana, D. Odermatt, I. Cesana, *et al.*, "Remote sensing of sun-induced chlorophyll-a fluorescence in inland and coastal waters: current state and future prospects," Remote Sens. Environ. **262**, 112482 (2021).
11. B. Nechad, K. G. Ruddick, and Y. Park, "Calibration and validation of a generic multisensor algorithm for mapping of total suspended matter in turbid waters," Remote Sens. Environ. **114**, 854–866 (2010).
12. J. Li, Q. Shen, B. Zhang, *et al.*, "Measurements and analysis of *in situ* multi-angle reflectance of turbid inland water: a case study in Meiliang Bay, Taihu Lake, China," Int. J. Remote Sens. **35**, 5167–5185 (2014).
13. http://lake.geodata.cn.
14. Y. Zhang, L. Zhang, C. Huang, *et al.*, "Dependence of the bidirectional reflectance distribution function factor f' on the particulate backscattering ratio in an Inland Lake," Remote Sens. **15**, 3392 (2023).
15. G. R. Fournier and J. L. Forand, "Analytic phase function for ocean water," Proc. SPIE **2258**, 194–201 (1994).
16. T. J. Petzold, "Volume scattering functions for selected ocean waters," Rep. 510, Ref. 72–78 (Scripps Institution of Oceanography, 1972).
17. D. Antoine, D. A. Siegel, T. Kostadinov, *et al.*, "Variability in optical particle backscattering in contrasting bio-optical oceanic regimes," Limnol. Oceanogr. **56**, 955–973 (2011).
18. K. M. Bisson, E. Boss, P. J. Werdell, *et al.*, "Particulate backscattering in the Global Ocean: a comparison of independent assessments," Geophys. Res. Lett. **48**, e2020GL090909 (2021).
19. M. Soja-Woźniak, M. Baird, T. Schroeder, *et al.*, "Particulate backscattering ratio as an indicator of changing particle composition in coastal waters: observations from great barrier reef waters," J. Geophys. Res. Oceans **124**, 5485–5502 (2019).
20. C. D. Mobley, "A numerical model for the computation of radiance distributions in natural waters with wind-roughened surfaces," Limnol. Oceanogr. **34**, 1473–1483 (1989).
21. J. D. Hedley and C. D. Mobley, "Hydrolight 6.0 Ecolight 6.0," (Numerical Optics Ltd, 2019).
22. D. McKee and A. Cunningham, "Evidence for wavelength dependence of the scattering phase function and its implication for modeling radiance transfer in shelf seas," Appl. Opt. **44**, 126 (2005).
23. C. D. Mobley, L. K. Sundman, and E. Boss, "Phase function effects on oceanic light fields," Appl. Opt. **41**, 1035 (2002).
24. A. Morel and B. Gentili, "Diffuse reflectance of oceanic waters. III. Implication of bidirectionality for the remote-sensing problem," Appl. Opt. **35**, 4850–4862 (1996).
25. R. W. Austin, "The remote sensing of spectral radiance from below the ocean surface," in *Optical Aspects of Oceanography*, N. G. Jerlov and E. Steemann-Nielsen, eds. (1974), pp. 317–344.
26. E. Aas and N. K. Højerslev, "Analysis of underwater radiance observations: apparent optical properties and analytic functions describing the angular radiance distribution," J. Geophys. Res. **104**, 8015–8024 (1999).
27. A. Morel, K. J. Voss, and B. Gentili, "Bidirectional reflectance of oceanic waters: a comparison of modeled and measured upward radiance fields," J. Geophys. Res. **100**, 13143 (1995).
28. C. Cox and W. Munk, "Slopes of the sea surface deduced from photographs of sun glitter," Bull. Scripps Inst. Oceanogr. **6**, 401–488 (1956).
29. T. Harmel, "Apparent surface-to-sky radiance ratio of natural waters including polarization and aerosol effects: implications for above-water radiometry," Front. Remote Sens. **4**, 1307976 (2023).
30. S. Mukherjee, J. D. Hedley, C. G. Fichot, *et al.*, "Optical closure in highly absorptive coastal waters: significance of inelastic scattering processes," Opt. Express **31**, 35178 (2023).
31. G. Zibordi and J.-F. Berthon, "Coastal atmosphere and sea time series (CoASTS) and bio-optical mapping of marine properties (BiOMaP): the CoASTS-BiOMaP dataset," Earth Syst. Sci. Data **16**, 5477–5502 (2024).